Journal of *Marine Science and Engineering*

MDPI

Article

Multi-Objective Optimization of TLP-FOWT Based on Surrogate Model

Zhenhao Song and Bo Woo Nam *

Department of Naval Architecture and Ocean Engineering, Seoul National University, Seoul 08826, Republic of Korea; songzhenhao@snu.ac.kr
* Correspondence: bwnam@snu.ac.kr; Tel.: +82-2-880-7324

Abstract

In this study, a systematic numerical study on design optimization was conducted for a tension leg platform (TLP)-type floating offshore wind turbine (FOWT), aiming to improve hydrodynamic performance, tendon behavior, and cost-effectiveness. Six design variables associated with hull geometry and tendon properties—pontoon length (PL), pontoon width (PW), platform draft (PD), main column diameter (CD), tendon pre-tension (Pre), and axial stiffness (EA)—were considered. For the global performance analysis, hydrodynamic coefficients were first obtained in the frequency domain, and motion and tendon tension responses were subsequently evaluated in the time-domain under a survival condition representative of a Southeast Asian site. A surrogate model based on the response surface method (RSM) was developed to predict platform responses across the design space. Multi-objective optimization was then performed using the non-dominated sorting genetic algorithm II (NSGA-II), yielding Pareto-optimal solutions that reveal trade-offs among competing performance metrics. The proposed framework is intended to provide Pareto-optimal design candidates for preliminary TLP-FOWT design, while the selection of a final design requires project-specific criteria and is beyond the scope of the present conceptual study. The optimization results show that the tendon tension can be effectively reduced while maintaining cost efficiency by increasing the pontoon length and slightly decreasing the tendon axial stiffness. For the tension–surge motion optimization, the Pareto-optimal solutions provide a balanced trade-off, where tendon tension is clearly reduced with only a slight increase in surge motion. In addition, the cost–nacelle acceleration optimization shows that nacelle acceleration can be further reduced by increasing the platform draft and pontoon length, although this is accompanied by a slight increase in the cost index. These findings provide practical insights for balancing global performance and cost in TLP-type FOWT design.

Keywords: genetic algorithm; TLP; response surface method; tendon tension; multi-objective optimization

Academic Editor: Decheng Wan

Received: 27 April 2026
Revised: 27 May 2026
Accepted: 28 May 2026
Published: 30 May 2026

1. Introduction

Over the preceding decades, the progression of offshore wind energy has experienced considerable evolution. According to the most recent report, the cumulative installed offshore wind capacity has experienced rapid growth, escalating from 90 MW in 2006 to 8771 MW by 2022, reflecting a persistent upward trajectory. Moreover, they also indicate an expected addition of over 380 GW of offshore wind capacity within the next 10 years [1]. To utilize the abundant wind resources in the deep-water area, several platforms have been

adopted as the supporting structures of the FOWTs. Among them, Semi-Submersible, TLP and Spar-type FOWT have been most widely installed in the past decades [1]. Compared to the other two floater concepts, which typically utilize taut or semi-taut mooring systems, the TLP employs a compliant floating platform moored to the seabed by several tendons. These tendons are pre-tensioned by excess buoyancy over the total structural and ballast weight. The tension leg platform (TLP) exhibits notably superior stability and vertical motion performance, encompassing heave, pitch, and roll, compared to Semi-Submersible, barge, and Spar platforms, owing to the use of pre-tensioned tendons that anchor the platform to the seabed, resulting in overall high-restoring forces in the vertical direction. Despite the excellent motion performance, TLP-type FOWTs are generally associated with high fabrication and installation costs, primarily due to the complexity of the pre-tensioned tendon system. Consequently, when conceptualizing the design of TLP-type FOWTs, striking an optimal balance between cost and hydrodynamic performance becomes challenging.

Many previous researchers have conducted the concept design and parametric studies of TLP-type FOWT in the past decades. Sclavounos et al. [2] carried out a parametric study of the design space for five single body FOWTs via fully coupled linear dynamic analysis in the frequency domain by coupling the LINES, WAMIT, and FAST codes. By comparing two different mooring systems—catenary lines with ballast and pre-tensioned tethers—they reported that both optimized mooring configurations lead to low nacelle acceleration RMS values, where the ballast catenary mooring system causes lower cost and the pre-tensioned tethers yield more motion resistance in deep water. Jagdale and Ma [3] developed a fast numerical time-domain model to simulate the dynamic behavior of the TLP-type FOWT under operational environmental conditions; the influence of alteration in platform configuration, such as variations in spoke size and the number of tendons, on the response of the system has been examined in detail. It was confirmed that the motion amplitude can be sufficiently reduced by increasing the number of tendons and increasing the length of spokes. Bachynski and Moan [4] investigated the design trends and considerations for single-column TLP-type FOWTs. They found that the tendon tension and platform motions are more influenced by variations in natural periods and stiffness rather than directly dependent on factors such as diameter, water depth, ballast fraction, or pontoon radius. Wang and Fan [5] compared six distinct TLP-type FOWTs with variations in spoke dimensions. Subsequently, by conducting model tests, comparisons were made among these models based on hydrodynamic coefficients such as added mass, damping, and response amplitude operators (RAO). It was observed that incorporating spoke dimensions alters the hydrodynamic characteristics, increasing added mass and slightly increasing pitch RAO values in the low-frequency range, while reducing them at higher frequencies.

In recent years, various optimization algorithms have been applied to the hull design of floating offshore structures to achieve optimal global performances. Sugita and Suzuki [6] introduced an optimization study focusing on hull sizing for TLP, with the objective of minimizing hull weight. By employing both genetic algorithm (GA) and simulated annealing algorithm (ASA) methodologies, they observed that under specified environmental conditions, with the constraints of tendon tension force and air-gap distance, the column diameter exhibited a significant influence on total hull weight. In particular, reducing the column diameter led to a noticeable decrease in hull weight, whereas variations in connecting pontoon dimensions had a smaller effect. Kim and Jang [7] developed a fully automatic assessment process including model generation, mass estimation, motion analyzer, and an optimization module based on the ASA method. By varying 11 design parameters and applying eight safety and installation constraints, they identified eight Pareto-optimal designs. Their results showed that both hull and tendon properties strongly

affect responses near the second peak frequency, with pontoon volume and tendon sectional area emerging as dominant factors. Placing greater weight on cost reduction led to smaller pontoon volumes and tendon areas, thereby lowering structural weight but increasing maximum heave response. Karimi et al. [8] carried out a global multi-objective optimization study involving three distinct types of FOWT (Spar, TLP, and Semi-Submersible) by using a multi-objective GA with the consideration of both the cost and nacelle acceleration. It was confirmed that below a cost of $4.5 M, both TLP and three-column Semi-Submersibles were optimal, whereas above this cost, TLP became the preferred option, although their hydrodynamic performance improved only slightly while costs rose sharply. Zhang et al. [9] proposed optimization research by applying NSGA-II to optimize the maximum dynamic tension and total platform weight of a multi-column TLP by tuning the hull draft, column spacing, column diameter, pontoon height, and pontoon weight. Their optimization results indicated that dynamic tendon tension increases with pontoon height and width but decreases with greater draft, column spacing, and column diameter. Park et al. [10] conducted systemic optimization work for a novel TLP-type FOWT with the consideration of multi-objectives including pitch motion and tendon tension responses. Via spectral analysis, they observed that the pitch motion of TLP design with small pretension and large EA could be effectively reduced in the wave-frequency ranges. Though the previous studies have provided valuable insights into the optimization of floating offshore structures, the simultaneous consideration of motion response, tendon loads and systematic cost-related performance still requires further investigation. In particular, for a TLP-type FOWT, the platform design should satisfy the vertical equilibrium condition, where the displacement, structural weight, ballast, and tendon pre-tension must be properly balanced with the consideration of cost individually.

In this study, a surrogate model-based multi-objective optimization framework was developed for a TLP-type floating offshore wind turbine (FOWT) to improve hydrodynamic performance, tendon behavior, and cost-effectiveness. The reference baseline platform was the NREL-TLP-FOWT [11], which consists of a single circular main column and four rectangular spokes. A met-ocean condition of a Southeast Asian region, including constant wind and survival wave scenarios, was adopted for the analysis. To improve computational efficiency, a surrogate model based on the response surface method (RSM) was developed to estimate hydrodynamic responses across the design space. Then a multi-objective optimization was performed using the NSGA-II algorithm to obtain Pareto-optimal designs. It should be noted that the objective of the present framework is to identify Pareto-optimal design candidates and clarify the trade-off relationships among competing objectives; the final selection of a single design configuration requires specific criteria, such as allowable tendon tension, nacelle acceleration limits, and budget constraints, and is therefore not prescribed in this study. In the proposed framework, the physical feasibility of the TLP design was ensured by considering the vertical equilibrium condition based on the balance among displacement, structural weight, ballast, and tendon pre-tension. The methodology for the Design of Experiment (DOE), surrogate model development, numerical analysis, and optimization process is described in Section 2, while the optimization results are presented in Section 3 and the conclusions are given in Section 4.

2. Numerical Method

Figure 1 illustrates a schematic diagram of the overall flow chart of the present study, encompassing key stages including initial design, Design of Experiment (DOE), frequency domain analysis, time-domain simulation, surrogate model construction, and multi-objective optimization. In the initial design stage, the design variables and their corresponding constraints were defined, and DOE was employed to generate represen-

tative sample points. Subsequently, frequency domain analyses were conducted using the commercial software ANSYS-AQWA (2023R1) to compute hydrodynamic coefficients (added mass and damping) and wave forces (exciting and drift forces) for all sample points. Time-domain simulations were then performed using OpenFAST [12], an open source aero-hydro-servo-elastic simulation tool developed by NREL (National Renewable Energy Lab). Based on the resulting motion responses and tendon tensions, an RSM-based surrogate model was constructed and its accuracy evaluated. Finally, multi-objective optimization was carried out using the NSGA-II algorithm, leading to the identification of various sets of optimal designs corresponding to different performance objectives.

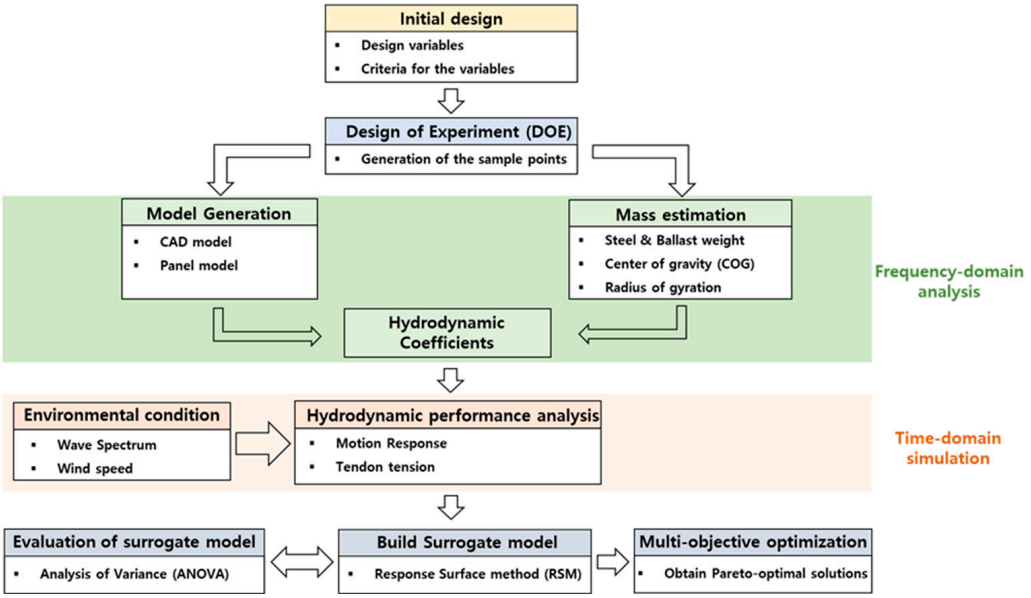

Figure 1. Flow chart of the overall optimization process.

2.1. Initial Design and Design of Experiment

The base platform used in this study is the NREL-TLP-FOWT [11], which is a conceptual design proposed by NREL (Figure 2). Table 1 presents the parameters related to its geometry, mass, and tendon system. The wind turbine employed is the 5-MW NREL wind turbine [13]. In this study, the blade and tower masses are assumed to remain constant across all design cases. The total weight of a TLP-type FOWT consists of several parts, including the steel weight of the platform, the ballast weight, and the weight of the upper structure (blades and tower). The approximate values for the steel weight of the platform hull were estimated based on assumed steel densities: 157 kg/m^3 for the upper main column, 224 kg/m^3 for the bottom main column, and 202 kg/m^3 for the pontoon [4], which is defined in Equation (1). The center of gravity for the platform hull was calculated based on the vertical distribution of steel weight in the upper and bottom main columns and pontoons (Figure 2). The radius of gyration was defined as a specific ratio of the gyration radius value that corresponds to a platform with homogeneous mass distribution: 57% in the roll and pitch direction, and 90% in the yaw direction. The ballast mass of a platform for each sample point was determined to satisfy the vertical static equilibrium among the tendon pre-tension, buoyancy, and weight of a structure. Regarding the capital cost of supporting the platform of a FOWT, in this work, a simplified cost estimation method was employed following Crozier's model [14], which approximates the total cost of a supporting platform by relating pre-tension force, steel weight, and ballast weight to fabrication costs.

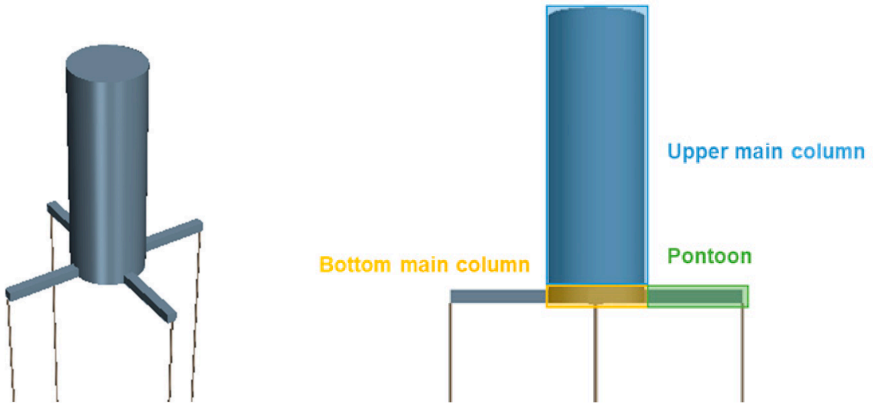

Figure 2. NREL-TLP-FOWT.

Table 1. Principal features of NREL-TLP-FOWT.

Property	Dimension
Platform radius (m)	9
Platform draft (m)	47.89
Pontoon length (m)	18
CM below still water level (m)	−40.61
Number of tendons (-)	4
Platform mass (kg)	8,600,000
Roll/Pitch moment of inertia ($kg * m^2$)	572,000,000
Tower height (m)	90
Tower mass (kg)	347,460
Upstretched tendon length (m)	151.73

To systematically generate sample points, a full factorial design approach was used to ensure that the surrogate model captures the full range of design variable interactions. In the DOE framework, design variables are referred to as 'factors', each of which can take on several different values known as 'level' [15], and the full factorial design approach explores all possible combinations of all factor levels. Table 2 lists the level distribution of six design variables: pontoon length (PL, x_1), pontoon width (PW, x_2), platform draft (PD, x_3), column diameter (CD, x_4), pre-tension force of each tendon (Pre, x_5), and axial stiffness (EA, x_6). It should be noticed that the factor level 3 for each variable corresponds to the base configuration (NREL-TLP-FOWT). As a result, a total of $5 \times 3^5 = 1215$ sample points were needed for direct evaluation. To guarantee physical feasibility, two hydrostatic constraints were imposed when generating valid sample designs. Since the total buoyancy force is primarily governed by the hull dimensions: pontoon length (PL), pontoon width (PW), platform draft (PD), and column diameter (CD), which directly determine the displacement of platform (∇) to achieve vertical static equilibrium, the first constraint ensures that the buoyancy must balance the total structural weight plus tendon pre-tension, resulting in a non-negative ballast mass ($m_{ballast}$), as expressed in Equation (3). Here, ρ_{water} denotes the water density, m_{plat} is the mass of the platform hull, and m_{WT} is the mass of the wind turbine. The second constraint limits the maximum ballast capacity: the required ballast volume should not exceed the available space inside the platform hull, which is determined by the draft, as formulated in Equation (4). Here, $\rho_{ballast}$ represents the ballast density. Design combinations that would require a negative ballast or an excessive ballast volume were therefore excluded.

$$m_{plat} = 157\pi x_4^2(x_3 - x_2)/4 + (56\pi x_4^2 x_2 + 808 x_2^2 x_1) \quad (1)$$

$$\nabla = \pi x_4^2 x_3/4 + 4x_2^2 x_1 \quad (2)$$

$$m_{ballast} = (\rho_{water} g \nabla - m_{plat} g - m_{WT} g - 4000 x_5)/g \geq 0 \quad (3)$$

$$m_{ballast}/(\pi x_4^2 \rho_{ballast}/4) \leq x_3 \quad (4)$$

Table 2. DOE of full factorial design.

Design Variable	Level 1	Level 2	Level 3	Level 4	Level 5
PL (m)	-	13	18	23	-
PW (m)	-	1.7	2.4	3.1	-
PD (m)	-	43.89	47.89	51.89	-
CD (m)	14	16	18	20	22
Pre/tendon (kN)	-	7000	8000	9000	-
EA/tendon (kN)	-	4,500,000	5,000,000	5,500,000	-

2.2. Frequency Domain Analysis

In the initial design stage, frequency domain hydrodynamic analysis was conducted to extract the hydrodynamic coefficients for each sample point design, including added mass, potential damping, and wave forces. Before proceeding to the time-domain simulations, a convergence test was carried out to determine the appropriate panel size. The panel model of the baseline NREL-TLP FOWT was utilized to check the convergence performance. Figure 3 presents the convergence results of added mass and potential damping for the pitch mode considering four different panel sizes. The differences among the results obtained using 3083, 6226, 9987, and 15,001 panels are mainly attributed to the discretization accuracy of the wetted surface in the potential-flow panel model. When the panel number is relatively small, the curved surfaces (side wall) of the main circular column as well as the corresponding pressure distribution on the wetted surface cannot be represented with sufficient accuracy. The differences in potential damping were found to be relatively minor, especially near the peak frequency (0.78 rad/s), indicating that panel size has little influence on the damping estimation of the present model. In contrast, the added mass values showed a clear decreasing trend with an increasing panel number from 3083 to 15,001. Notably, this reduction became negligible when the panel number exceeded 6226. Consequently, a panel size of 0.6 m was selected for all sample points throughout this study to ensure a balance between numerical accuracy and computational efficiency, corresponding to a panel number of 6226.

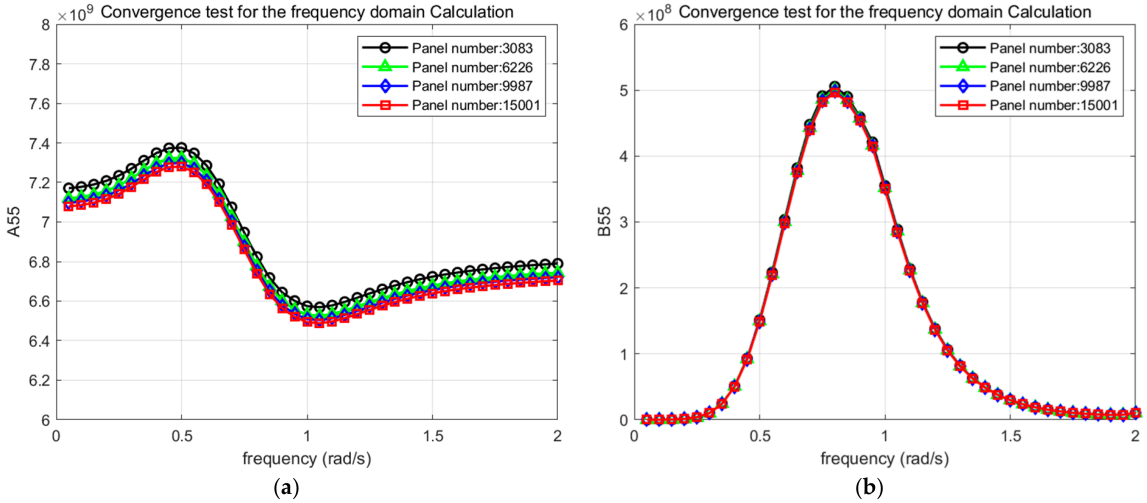

Figure 3. Convergence test for the panel model of NREL-TLP FOWT: (**a**) added mass; (**b**) potential damping.

2.3. Environment and Time-Domain Simulation

In this study, a survival met-ocean condition for a Southeast Asian area was selected as the target environmental condition [6]. The irregular wave condition was characterized by a peak period of 15 s and a significant height of 9 m, based on the Pierson–Moskowitz spectrum (Figure 4). Additionally, a constant wind speed (24 m/s) was employed and the wind turbine was assumed as a parked condition.

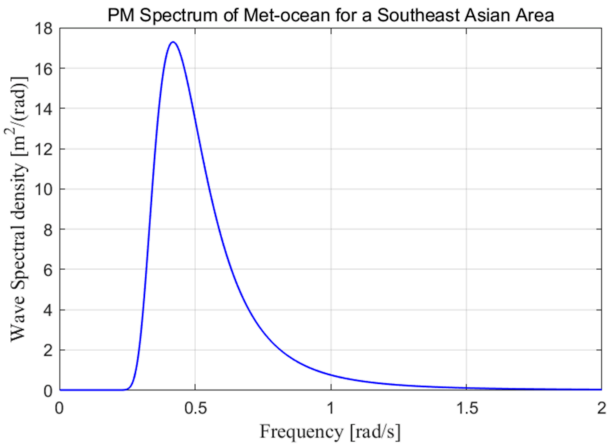

Figure 4. Survival met-ocean condition for a Southeast Asian Area (H_s: 9 m, T_p: 15 s).

In HydroDyn module of FAST, the motion responses of TLP-type FOWT were calculated through a nonlinear time-domain simulation framework and Cummins' theory [16], with the motion equations given in Equation (5):

$$\begin{array}{l}[M_{PLATmn} + M_{WTmn} + A(\infty)_{mn}]\ddot{x}_n(t) \\ + \int_{-\infty}^{t} H_{mn}(t-\tau)\dot{x}_n(t)d\tau + [K_{mn} + K_{TENDON_{mn}}(t)]x_n(t) = F_{WAVE_n}(t) + F_{WIND_n}(t) + F_{WaveDrift_n}(t); \\ m, n \\ = 1, 2, \ldots 6\end{array} \quad (5)$$

Here, M_{PLAT}, M_{WT}, and $A(\infty)$ denote the mass of platform, mass of entire wind turbine, and infinite-frequency added mass coefficient matrix, respectively. K and $K_{TENDON}(t)$ are the hydrostatic coefficient matrix and additional stiffness forces due to the tendon tension, respectively. $F_{WAVE}(t)$ and $F_{WaveDrift}(t)$ represent the first-order wave exciting force and second-order wave drift force acting on the platform, respectively. F_{WIND} is the steady wind force. In this study, Newman's approximation method was applied to compute the second-order wave drift forces. The convolution integral in the second term denotes the memory effect of a free surface, where H(t) is the retardation function matrix derived from the added mass and damping coefficients in frequency domain by applying Kramer–Kronig relations based on the Fourier transform [17] as in the following (Equation (6)):

$$\begin{aligned} H(t) &= -\frac{2}{\pi}\int_0^\infty \omega(A(\omega) - A(\infty))\sin(\omega t)d\omega \\ &= \frac{2}{\pi}\int_0^\infty C(\omega)\cos(\omega t)d\omega \end{aligned} \quad (6)$$

where $A(\omega)$ is the added mass coefficient and $C(\omega)$ signifies the potential damping coefficient. In this study, linear viscous damping has been introduced into the surge, heave, and pitch motions, with damping ratios of 2.5%, 1%, and 1%, respectively, based on the experimental measurements reported by Vardaroglu et al. [18]. In Equation (7), the upper

limit of integration term can be truncated at a finite cut-off wave frequency ω_{max}, and corresponding retardation function could be described as Equation (7):

$$H(t) = \frac{2}{\pi}\int_0^{\omega_{max}} C(\omega)\cos(\omega t)d\omega \tag{7}$$

In addition to the linear additional damping matrix, nonlinear viscous drag loads are also calculated in the HydroDyn module by using Morison's equation with a strip approach. Drag forces are computed for each segment individually and then integrated over the brace member length to obtain the total force. In HydroDyn, the Morison's equation for the surge and sway modes of motion was given as below [19]:

$$\begin{gathered} dF_i^{Platform}(t,z) = -C_A\rho\left(\frac{\pi D^2}{4}dz\right)\ddot{q}_i(z) + (I + C_A)\rho\left(\frac{\pi D^2}{4}dz\right)a_i(t,0,0,z) + \\ \frac{1}{2}C_D\rho(Ddz)\left[v_i(t,0,0,z) - \dot{q}_i(z)\right]\left|v(t,0,0,z) - \dot{q}(z)\right|;\ \text{for } i = 1\text{or}2 \end{gathered} \tag{8}$$

where D is the characteristic diameter of the cylinder and dz is the length of the differential segment along the brace member. C_A and C_D represent the normalized hydrodynamic added mass and viscous drag coefficients of each member. v_i and a_i denote the undisturbed fluid-particle velocity and acceleration in the direction i. Three terms in Equation (8) are the inertia forces due to the added mass, the inertia forces due to the member's own displaced mass and the viscous drag load acting on the brace member, respectively. C_D for the platform and the pontoons of all sample points are determined as 0.7 referring to the baseline NREL-TLP. It should be noted that the first term (C_A) in Equation (8) is not taken into account in present strip approach, since the added mass has already been considered by the calculations in frequency domain.

To further confirm the reliability of the present numerical model, the motion responses of the TLP-type FOWT were additionally compared with the previously published experimental and numerical results reported by Vardaroglu et al. [18]. It should also be noted that the tendon axial stiffness is different between the two models, with values of 14.7 MN/m in DHI-TLP [18] and 20 MN/m in the present NREL-TLP model [11]. In addition, the platform displacement is 12,696 m^3 in the DHI-TLP model and 12,187 m^3 in the present NREL-TLP model. Figure 5 compares the surge, heave, and pitch RAOs obtained from the present time-domain analysis with the corresponding experimental and numerical results reported by Vardaroglu et al. [18]. It is evident that the present results show reasonable agreement with the benchmark data in terms of the overall response trends under various wave frequencies, despite some discrepancies that may be attributed to differences in numerical and experimental conditions. Overall, the comparison confirms that the present time-domain simulations are capable of capturing the motion response of the single-body TLP-type FOWT and are therefore applicable to the subsequent optimization study.

In this study, 3 h time-domain simulations were conducted for all design cases using OpenFAST, with a fixed time step of 0.01 s. The initial transient stage was treated by removing the first 1000 s, and the maximum response quantities, including surge motion, nacelle acceleration, and tendon tension, were extracted from the effective simulation time window between t = 1000 and t = 10,800 s. The tendon system was modeled using the FEAMooring module. FEAMooring is a finite-element-based mooring dynamics module, in which each tendon is discretized into line elements and the corresponding fairlead reaction forces are calculated during the time-domain simulation. In the present TLP model, the tendons were defined as vertical tension members by specifying the anchor and fairlead positions, unstretched tendon length, mass properties, initial pre-tension, and axial stiffness. It is worth noting that our previous study demonstrated that the selected wave seed can have an influence on the absolute maximum response values obtained from stochastic

time-domain simulations [10]. Nevertheless, the relative design trends among different platform configurations were found to remain generally consistent under different wave seeds. Based on this observation, the present study adopted one representative wave seed for all design candidates under the same environmental condition. This approach enables a consistent comparative assessment of the design candidates by eliminating additional variability associated with different stochastic wave realizations. Therefore, the absolute maximum response values reported in this study may still contain seed-dependent uncertainty. However, it should be noted that the main objective of the present optimization is to identify the relative design trends and Pareto-optimal design characteristics among different TLP-FOWT configurations, rather than to determine statistically converged extreme response values.

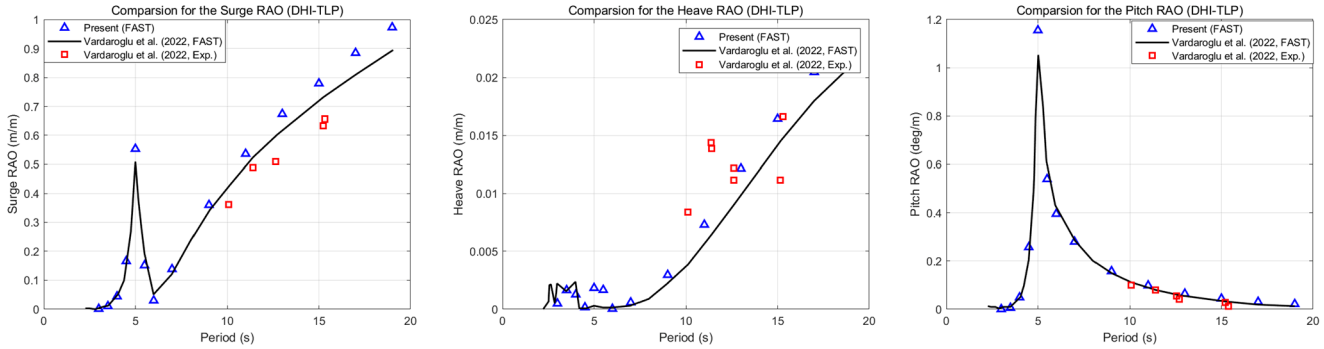

Figure 5. Validation of the RAO of TLP-type FOWT under regular waves: (**a**) Surge; (**b**) Heave; (**c**) Pitch [18].

2.4. Surrogate Model and NSGA-II Algorithm

When using the NSGA-II algorithm to explore the optimal design space, it is computationally impractical to conduct the hydrodynamic simulations for every candidate solution directly. To improve overall computational efficiency, a surrogate model was employed to predict the hydrodynamic performances of all the sample designs of TLP-type FOWTs. An RSM [20] has been introduced to build the relationship between the inputs (design variables) and outputs (motion responses and tendon tensions), capturing potential interaction effects among design variables. Commonly, two types of mathematical models are widely used in RSM, including the first-order model (Equation (9)) and the second-order model (Equation (10)). To identify the most suitable RSM model, the prediction performances of the first-order model, second-order model (without interaction terms), and second-order model were tested, with the corresponding formulations shown in Table 3. The prediction performances of three RSM models are illustrated in Figure 6. The results confirmed that the second-order model (Figure 6a) exhibited a superior predictive performance compared to the other two types of RSM models, demonstrating that the interaction effects between different design variables are significant and cannot be ignored. Consequently, the second-order model was employed to estimate various motion and tension responses throughout this research.

In this work, the standard deviation and maximum values of the tension force (T_1), surge motion (ξ_1), pitch motion (ξ_5), and nacelle acceleration were selected as the objective functions, as these parameters are directly associated with the safety of tendon lines and the dynamic stability of the platform. The predictive performance of the adopted surrogate model with respect to different objective functions is depicted in Figure 7.

$$y = \beta_0 + \sum_{i=1}^{k} \beta_i x_i + \epsilon \tag{9}$$

$$y = \beta_0 + \sum_{i=1}^{k} \beta_i x_i + \sum\sum_{i<j} \beta_{ij} x_i x_j \sum_{i=1}^{k} \beta_{ii} x_{ii}^2 + \epsilon \quad (10)$$

Table 3. Three different RSM models.

RSM Model	Formula
First-order model	$y = a_1 + a_2x_1 + a_3x_2 + a_4x_3 + a_5x_4 + a_6x_5 + a_7x_6$
Second-order model (w/o interaction terms)	$y = a_1 + a_2x_1 + a_3x_2 + a_4x_3 + a_5x_4 + a_6x_5 + a_7x_6 + a_8x_1^2 + a_9x_2^2 + a_{10}x_3^2 + a_{11}x_4^2 + a_{12}x_5^2 + a_{13}x_6^2$
Second-order model	$y = a_1 + a_2x_1 + a_3x_2 + a_4x_3 + a_5x_4 + a_6x_5 + a_7x_6 + a_8x_1^2 + a_9x_2^2 + a_{10}x_3^2 + a_{11}x_4^2 + a_{12}x_5^2 + a_{13}x_6^2 + a_{14}x_1x_2 + a_{15}x_1x_3 + a_{16}x_1x_4 + a_{17}x_1x_5 + a_{18}x_1x_6 + a_{19}x_2x_3 + a_{20}x_2x_4 + a_{21}x_2x_5 + a_{22}x_2x_6 + a_{23}x_3x_4 + a_{24}x_3x_5 + a_{25}x_3x_6 + a_{26}x_4x_5 + a_{27}x_4x_6 + a_{28}x_5x_6$

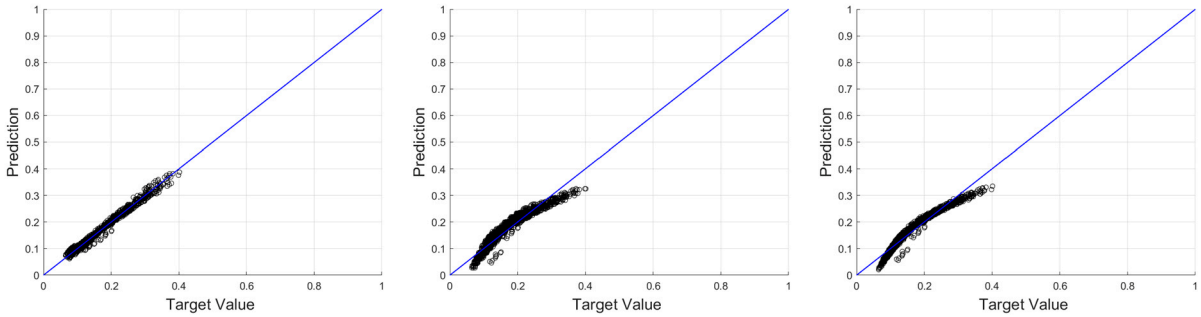

Figure 6. Prediction results of RSM w.r.t three different models: (**a**) Second-order model; (**b**) Second-order model without interaction terms; (**c**) First-order model.

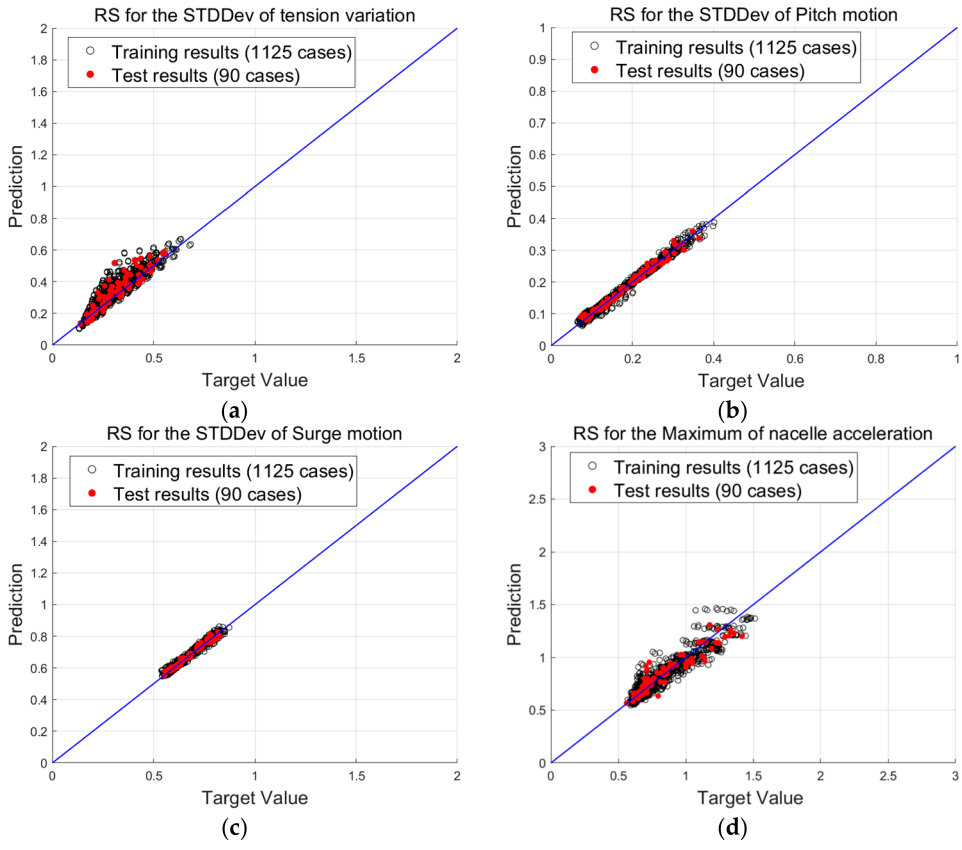

Figure 7. Prediction results via Second-order model: (**a**) tension variation; (**b**) pitch motion; (**c**) surge motion; (**d**) nacelle acceleration.

Additionally, the fitness of the RSM-based surrogate model was systematically evaluated using the analysis of variance (ANOVA) method. The central concept of ANOVA is to compare the variation attributed to the treatment, which involves changes in the combination of variable levels, with the variation arising from random errors inherent in the measurements of the generated responses [21]. This comparison enables the evaluation of the significance of the regression employed to predict responses while considering the sources of experimental variance.

Table 4 lists the evaluation of the significance of regression for the three surrogate models utilized in this research. The significance of regression can be evaluated by the ratio between the media of the square of regression (MSreg) and the media of the square of residuals (MSres) and by comparing these variation sources using Fisher distribution (F test), considering their respective degrees of freedom for regression (model) and to residual (error) variances. This ratio must be higher than the tabulated value for F [22]. Based on Table 4, it is evident that the F-values for the present three surrogate models are substantially greater than the critical F-value, indicating that there is just an error or risk of 0.01% to reject the null hypothesis which is true, in other words, the present mathematical models are well fitted to the simulation data within the investigated DOE space. It should be noted that the ANOVA-based F-test is used here as a within-DOE statistical diagnostic for evaluating the regression significance of the RSM surrogate models. Therefore, the validity of the developed surrogate models is bound by the DOE coverage, the prescribed design-variable ranges, and the specified environmental condition shown in Figure 4. If the sea state, water depth, or operating condition is changed, the numerical database should be regenerated and the corresponding surrogate model should be reconstructed.

Table 4. ANOVA evaluation of surrogate models.

	Source	Sum of Squares	Degree of Freedom	Mean Square	F-Value	Critical F-Value (Significance Level = 0.01)	P > F
Tension	Model	15.7419	27	5.83×10^{-01}	9636	2.1	<0.0001
	Error	0.0718	1187	6.05×10^{-05}			
	Total	15.8137	1214	-			
Surge	Model	2.7713	27	1.03×10^{-01}	3815	2.1	<0.0001
	Error	0.0321	1187	2.70×10^{-05}			
	Total	2.8034	1214	-			
Pitch	Model	11.4704	27	4.29×10^{-01}	1950	2.1	<0.0001
	Error	0.2611	1187	2.20×10^{-04}			
	Total	11.8315	1214	-			

Finally, with the application of the present RSM-based surrogate models, the final optimization work was conducted using the NSGA-II algorithm (Figure 7). Here, P_t denotes the parent population of TLP-FOWT individuals in generation t, and in the same generation, Q_t is the offspring population of TLP-FOWT individuals generated from P_t by applying genetic operators (selection, crossover, and mutation) to change the design parameters (PL, PW, PD, CD, Pre, and EA). NSGA-II (Figure 8) is a well-established multi-objective optimization algorithm that extends the classical genetic algorithm to address problems with multiple conflicting objectives [23]. Different from the conventional optimization algorithm, after the cross-over process, "non-dominated sorting" and "crowding distance sorting" are employed to individuals for selecting the next generation. "Non-dominated sorting" categorizes individuals into different fronts based on their dominance relationships.

Individuals in the first front are non-dominated by any other individual in the population, those in the second front are dominated only by individuals in the first front, and so on. "Crowding distance sorting" assigns a crowding distance to each individual within each front, measuring how crowded an individual is among its neighbors in the objective space. Individuals with larger crowding distances are preferred for selection to maintain diversity in the population. By efficiently maintaining a diverse set of non-dominated solutions throughout the entire optimization process, NSGA-II provides a group of Pareto front solutions which optimize conflicting objectives.

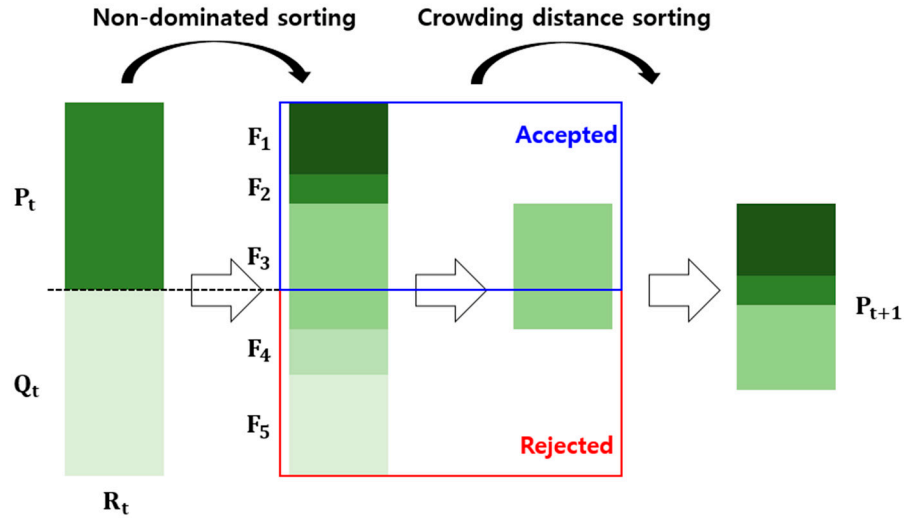

Figure 8. Schematic diagram for non-dominated sorting genetic algorithm II (NSGA-II).

3. Results and Discussion

3.1. Optimization of Tension and Surge Motion

In this section, an optimization study was conducted considering the dual objectives of tendon tension and surge motion, as illustrated in Figure 9. The figure presents both the maximum surge motion and maximum tension force for all designs as non-dimensional values, normalized by the corresponding values of the initial baseline design. To ensure the convergence of the optimization process, the number of iterations (generation number) was set as 5000 with a population size of 25 individuals per generation. Black circle symbols are the sample points, the red diamond symbol represents the initial baseline design (NREL-TLP-type FOWT), and the blue square symbols denote the Pareto-optimal designs identified through the NSGA-II optimization process, each of which is non-dominated by the others. Overall, the group of Pareto-optimal designs demonstrated improved performance, with reductions in both maximum tendon tension and surge motion compared to the initial NREL-TLP design. Specifically, when comparing two representative edge solutions on the Pareto front (Solution 26 and Solution 50) with the baseline design, Solution 26 exhibited a 29.4% reduction in surge motion but a 0.9% increase in maximum dynamic tension force, while Solution 50 showed reductions of 15.1% and 22.9% in dynamic tension and surge motion, respectively. The distribution of Pareto-optimal solutions for surge–tension optimization exhibits a dispersed and homogeneous spread. This broader distribution suggests the absence of a single dominant trade-off region, indicating that a wider range of design variable configurations can achieve a favorable balance between surge motion and maximum dynamic tension force under the considered survival sea states.

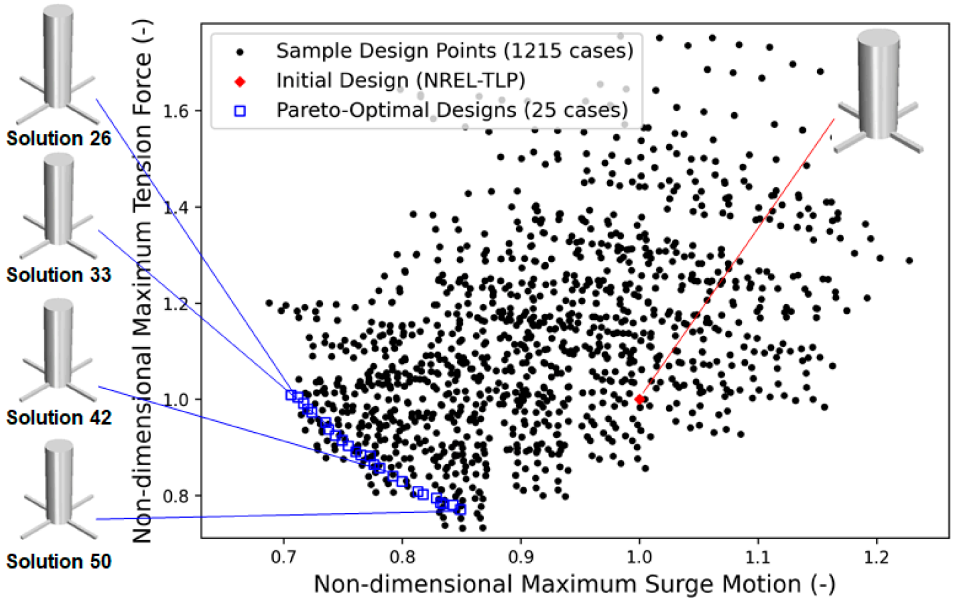

Figure 9. Optimization results based on the consideration of tension–surge evaluation: Pareto-optimal solutions by NSGA-II.

The distribution of the design parameters of Pareto-optimal solutions (Figure 10a) reveals that platform draft and pre-tension force play critical roles in influencing the dynamic response. Specifically, an increase in platform draft significantly enhances the hydrodynamic added mass, damping, and viscous drag forces, which leads to decreasing surge motion. Conversely, a reduction in draft increases the effective stretching length of the tendons. Longer tendons soften the restoring behavior of the platform in the vertical direction, leading to reduced axial stiffness and lower peak tension forces. Additionally, the surge motion of the platform is also mitigated due to the reducing drag forces in the surge direction. However, the present Pareto-optimal solutions demonstrate that the response behaviors result from the combined effects of draft, pre-tension force, and pontoon length (Figure 10a), which simultaneously alter the hydrostatic and hydrodynamic characteristics. Except for the effect of draft, a lower pre-tension force reduces the mean tension level in the tendon system, further contributing to the overall decrease in maximum dynamic tension force. Since increasing the column diameter amplifies wave excitation forces acting on the platform, it leads to larger surge motion amplitudes and correspondingly higher maximum tendon tension forces. As a result, all Pareto-optimal solutions tend to fix the column diameter at its lower bound to mitigate both the maximum surge motion and dynamic tension force. Meanwhile, the pontoon width remains near its minimum value across all optimal designs, reflecting its relatively minor influence on surge–tension behavior within the explored design space. Additionally, the variation in pontoon length among the optimal designs exhibits a non-monotonic trend, implying a more complex influence of pontoon geometry on surge-induced tension loads, which suggests that pontoon length could simultaneously influence the restoring characteristics and drag forces due to the overall configurations.

Furthermore, the comparison of the time series for the surge motion (ξ_1) and tendon tension force (T_1) is illustrated in Figure 11, which was obtained from direct OpenFAST re-simulations of the selected Pareto-optimal designs. For solution 50, both surge motion and dynamic tendon tension exhibited reduced values throughout the time window relative to the initial design. In contrast, Solution 26 demonstrated a significant reduction in surge motion but also experienced an increase in tendon tension compared to the baseline configuration, resulting from the larger pre-tension, which could also be clearly observed

from the time history and corresponding spectra (Figure 11). In addition to the magnitude of oscillation, there is also a noticeable decrease in mean value, finally leading to a remarkable reduction in the peak value of the surge motion. Consequently, these optimal results indicate that by appropriately adjusting platform draft and tendon pre-tension, a TLP-type FOWT design can be achieved that optimally balances surge response and dynamic tension.

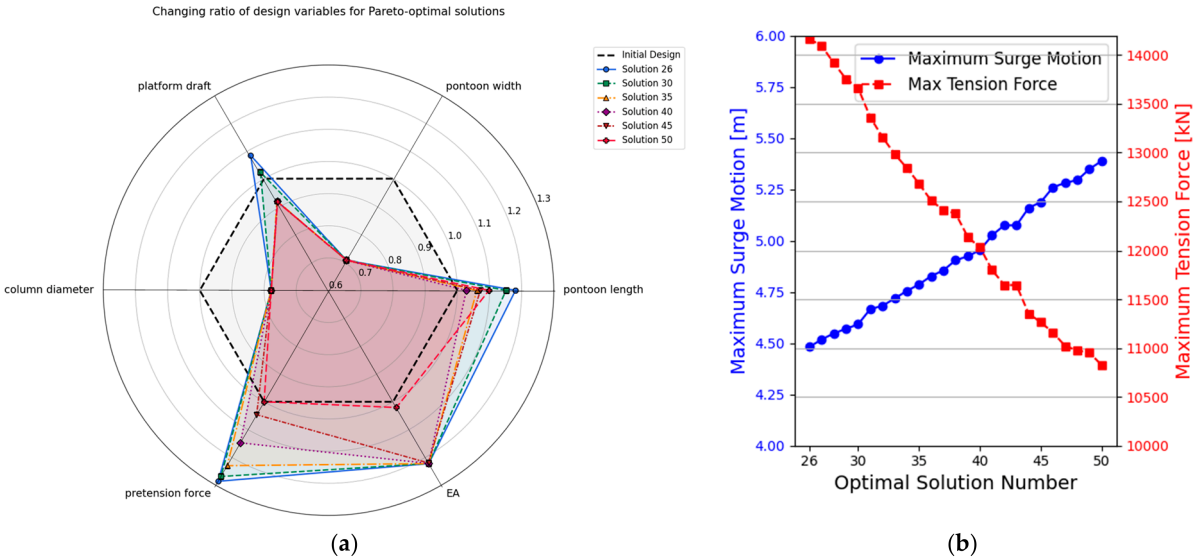

(**a**) (**b**)

Figure 10. Distribution of design parameters of Pareto-optimal solutions: (**a**) Design variables; (**b**) Objective values.

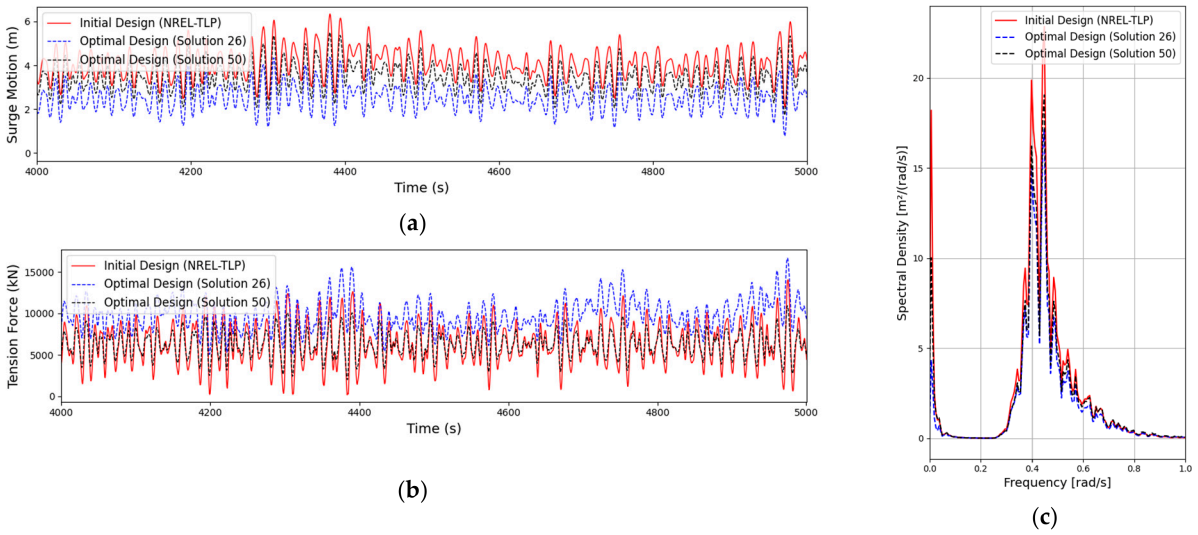

(**a**) (**b**) (**c**)

Figure 11. Comparison of the time series and spectra between optimal Solutions (Solution 26 and Solution 50) and initial design: (**a**) surge motion; (**b**) tension force of upstream tendon; (**c**) motion response spectra.

3.2. Optimization of Tension and Cost

In this section, optimization was conducted by utilizing the NSGA-II algorithm in conjunction with a pre-built surrogate model, considering both tendon tension and cost index as the objective functions. The optimization results are illustrated in Figure 12. Overall, the set of optimal designs demonstrates improved performance in terms of both reduced tendon tension forces and lower cost estimates relative to the initial NREL-TLP design. Specifically, when comparing two representative extreme solutions of the Pareto front (Solution 1 and Solution 25) with the baseline design, Solution 1 achieved reductions

of 16.8% in maximum dynamic tension force and 35.1% in cost index, while Solution 25 showed reductions of 22.9% and 34.5%, respectively. The clustering pattern of the Pareto-optimal solutions indicates the existence of a narrow design region, wherein tendon performance under survival sea states can be improved without significantly compromising economic feasibility.

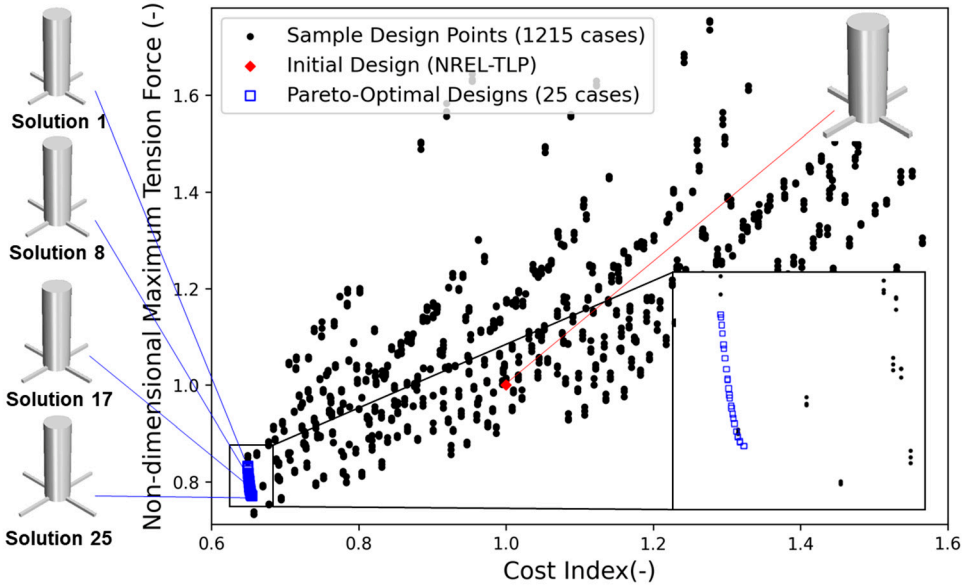

Figure 12. Optimization results based on the consideration of tension-cost evaluation: Pareto-optimal solutions by NSGA-II.

The analysis of design parameter trends (Figure 13) indicates that two variables—pontoon length and axial stiffness (EA)—play a particularly dominant role in influencing the dynamic tension response. Figure 14 compares the time histories of tendon tension force (T_1) for two optimal solutions (Solution 1 and Solution 25) and the baseline design, which were obtained from direct OpenFAST re-simulations of the selected Pareto-optimal designs. The results further confirm that the optimized configuration with long pontoon length and small axial stiffness yields substantially lower peak values of dynamic tension forces throughout the time window. Furthermore, under the same pre-tension level of 7000 kN, the optimized designs also exhibit a markedly reduced standard deviation in dynamic tension force, since the longer pontoon length enhances the restoring arm of the platform, thereby suppressing pitch and surge motions. As illustrated in Figures 14 and 15, this reduction in platform motion directly contributes to the mitigation of maximum dynamic tendon tension, since pitch motion significantly amplifies tendon loads. Conversely, a reduction in EA slightly increases the surge and pitch motions due to decreased restoring forces. Moreover, the reduction in axial stiffness allows the tendons to undergo greater elongation during dynamic loading, which further decreases the total effective stiffness of the tendon. This behavior is further illustrated in Figure 16, which compares the maximum responses of three sample designs (cases 1, case 82, and case 163) with progressively increasing EA values, while holding the other five design variables constant. This increased flexibility helps to spread out force transmission over time, slightly reducing sharp tension peaks in the tendons. This adjustment of the hull dimensions and tendon stiffness proves particularly effective in mitigating peak tension loads under extreme sea conditions. In contrast, other parameters such as pontoon width, pre-tension force, platform draft, and column diameter, showed limited variation across the Pareto-optimal solutions, indicating a relatively minor role in influencing the dynamic tension response. In the optimal solutions, the pontoon width remained at its lower bound, as it has limited influence on hydrodynamic motion

response while contributing to an increase in structural cost. Similarly, pre-tension force was minimized, owing to its dominant effect on both mean and peak dynamic tension responses. It should be noted that although platform draft and column diameter settled at their lower bounds, this trend reflects their substantial contribution to platform cost, rather than a lack of influence on performance. Overall, present Pareto-optimal solutions offer valuable guidance for the preliminary design of TLP-type FOWTs, indicating that an appropriate increase in pontoon length—which effectively increases the fairlead arm length—with a slight decrease in axial stiffness (EA) can achieve substantial reductions in dynamic load responses at a minimal cost.

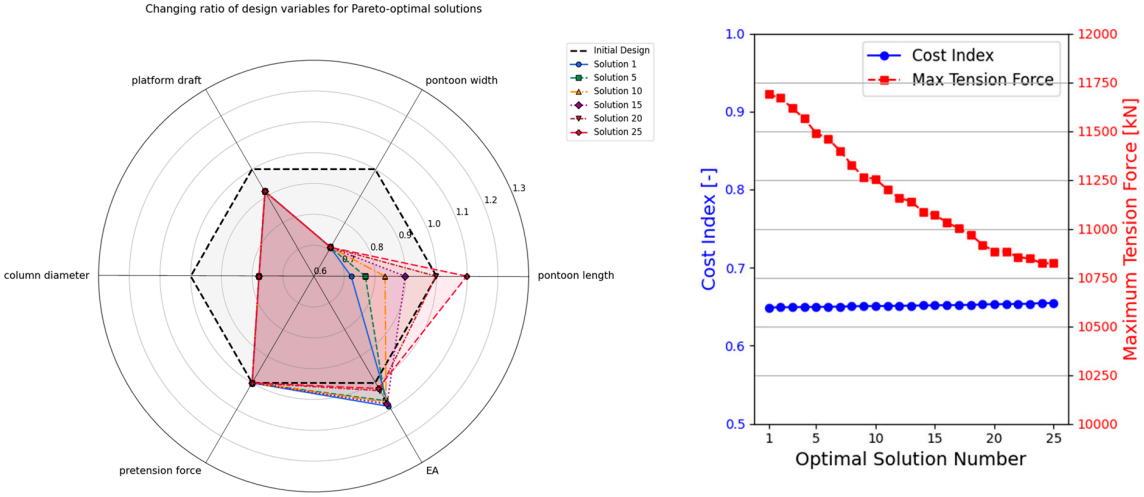

Figure 13. Distribution of design parameters of Pareto-optimal solutions: (**a**) Design variables; (**b**) Objective values.

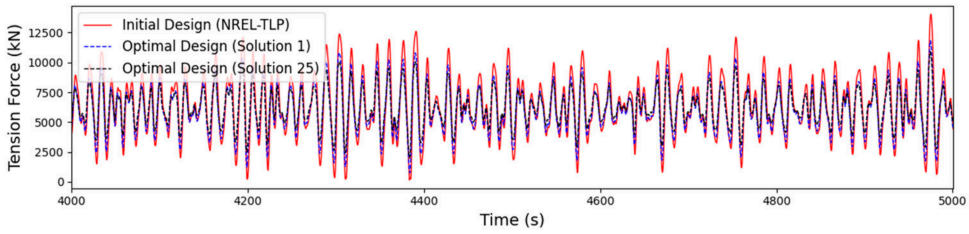

Figure 14. Comparison of the time history between optimal solutions (Solution 1 and Solution 25) and initial design.

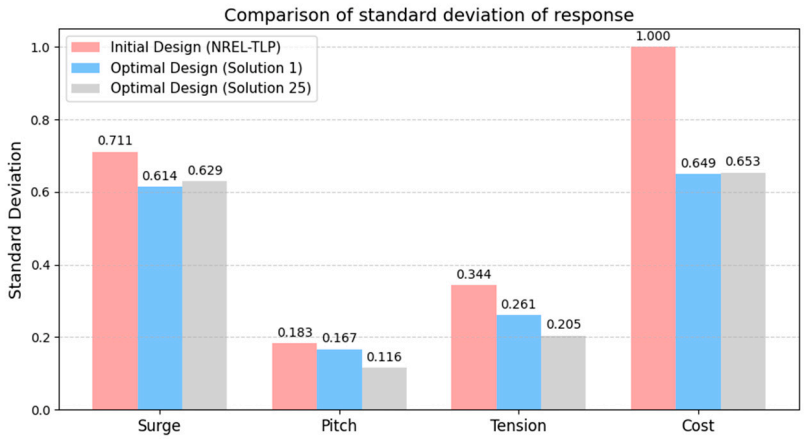

Figure 15. Comparison of motion standard deviation between optimal solutions (Solution 1 and Solution 25) and initial design.

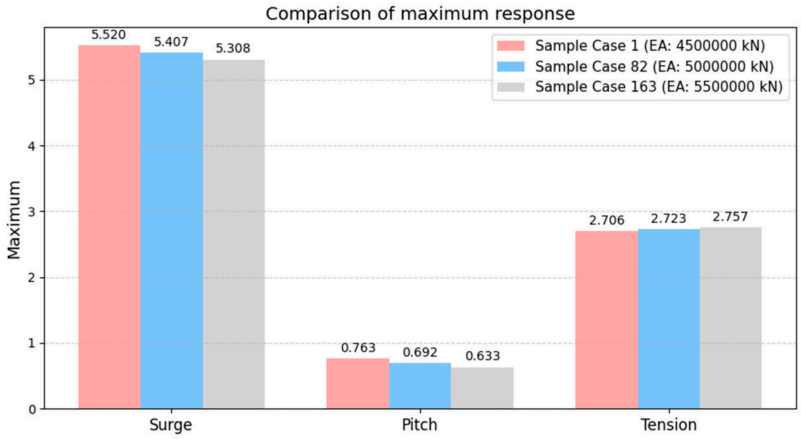

Figure 16. Comparison of effect of EA on maximum motion response.

3.3. Optimization of Nacelle Acceleration and Cost

Since excessive nacelle accelerations can shorten the service life of critical turbine components or even trigger the failure of acceleration-sensitive parts [24], nacelle acceleration has been widely seen as a critical parameter in assessing the dynamic performance of FOWT platforms. In this section, an optimization study was conducted considering the dual objectives of cost index and nacelle acceleration, as illustrated in Figure 17. Similarly, the maximum nacelle acceleration for all designs are presented as non-dimensional values, normalized by the corresponding values from the initial baseline design. Compared to the baseline NREL-TLP configuration, the set of optimal designs achieved reductions in both nacelle acceleration and overall cost index. Specifically, when comparing two representative edge solutions on the Pareto front (Solution 51 and Solution 75) with the baseline design, Solution 51 exhibited a 2.3% increase in maximum nacelle acceleration and a 35.1% reduction in cost index, while Solution 75 showed reductions of 26.9% in nacelle acceleration and 30.2% in cost index.

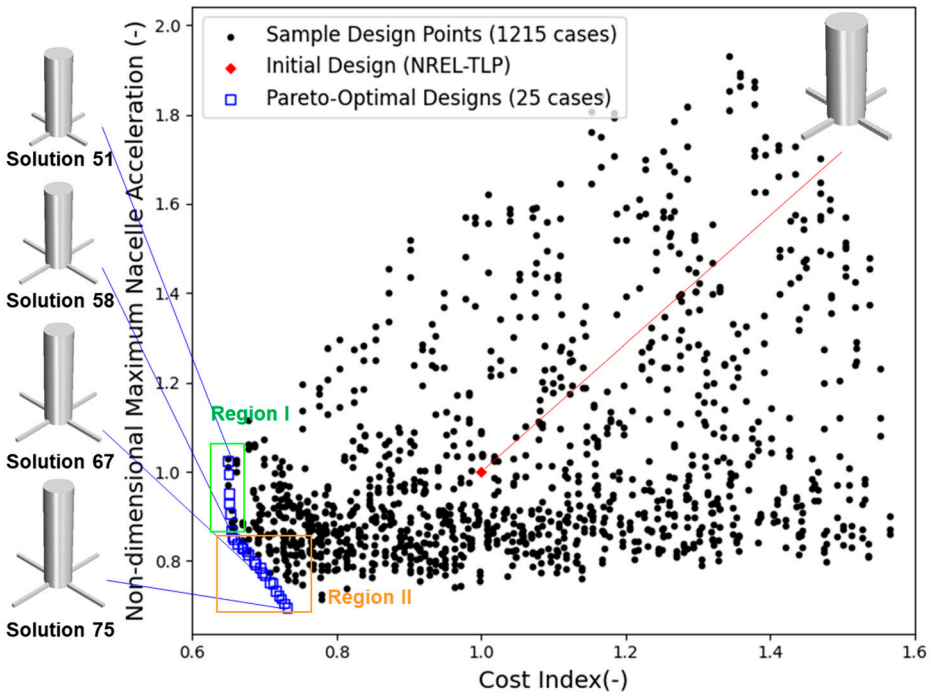

Figure 17. Optimization results based on the consideration of cost–nacelle acceleration evaluation: Pareto-optimal solutions by NSGA-II.

The Pareto front for the cost–nacelle acceleration optimization reveals trade-off characteristics across the optimal solution space, where two extreme regions ensure either a minimum cost index or a minimum nacelle acceleration. As shown in Figure 18, in the first region near Solution 51, the cost index reaches its minimum with only a modest reduction in nacelle acceleration. This cost-dominated improvement is primarily achieved by minimizing design variables that strongly affect cost but have limited influence on dynamic response. Specifically, pontoon width, column diameter, and pre-tension force are consistently fixed at their lower bounds in this region. Meanwhile, pontoon length exhibits a sharp increase toward its upper bound, indicating its crucial role in enhancing restoring moments and reducing pitch motion. In the region near Solution 75, nacelle acceleration shows a remarkable decrease while the cost index slightly increases. This improvement is mainly attributed to a continued increase in pontoon length, along with a gradual increase in platform draft. The increased draft enhances added mass, damping, as well as drag force in both surge and pitch directions, thereby reducing motion-induced nacelle acceleration. Notably, the axial stiffness (EA) is maintained at its upper bound throughout both regions, suggesting its importance in constraining overall motion responses required to limit nacelle displacement under survival sea state. Figure 19 further illustrates the relationship among three dynamic responses: surge, pitch, and nacelle acceleration. The results are shown for three sample designs (case 1, case 28, and case 56) in which the pontoon length progressively increases, while the other five design variables remain constant. It was confirmed that although the surge motion of TLP hull increases with longer pontoon length, the nacelle acceleration of FOWT continuously decreases with reducing pitch motion, which implies that the pitch motion significantly affects the nacelle acceleration of the FOWT. Finally, Figure 20 compares the time histories of nacelle acceleration for an optimal solution (Solution 75) and the baseline design, which were obtained from direct OpenFAST re-simulations of the selected Pareto-optimal designs. The time series shows that the optimized design (Solution 75) produces overall smaller peak values of nacelle acceleration throughout the time window. Present optimization results highlight the dominant role of pontoon length in the initial stage of acceleration mitigation, followed by a more distributed contribution from the platform draft and overall hull configuration as cost reduction becomes more important.

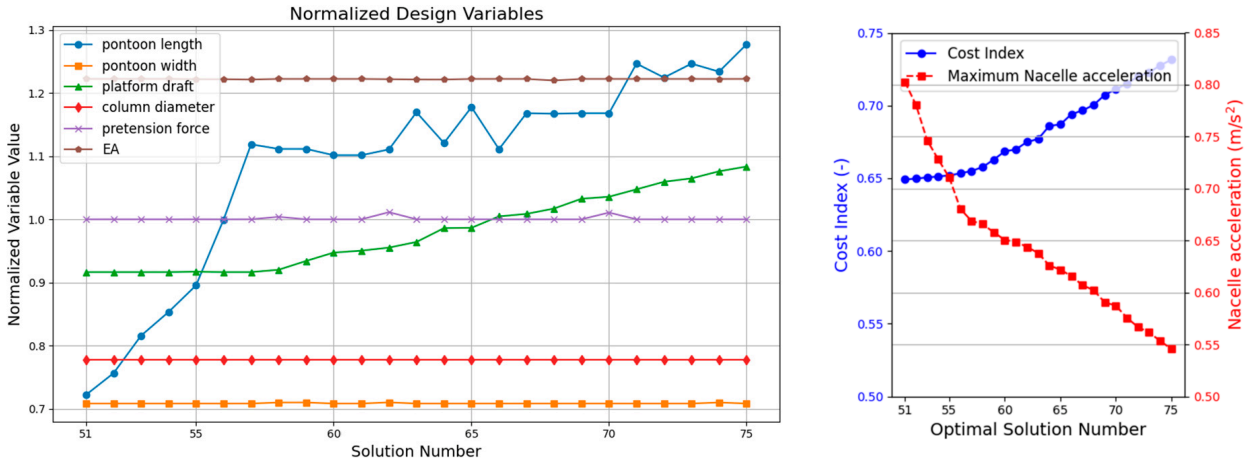

(**a**) (**b**)

Figure 18. Distribution of design parameters of Pareto-optimal solutions: (**a**) Design variables; (**b**) Objective values.

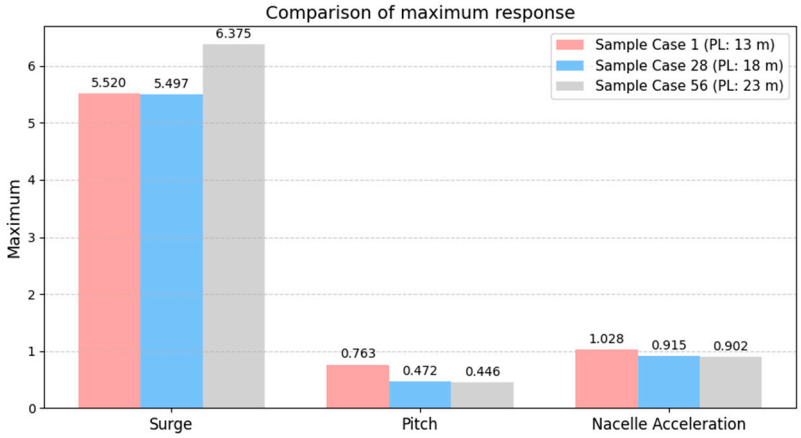

Figure 19. Comparison of effect of pontoon length on maximum motion response.

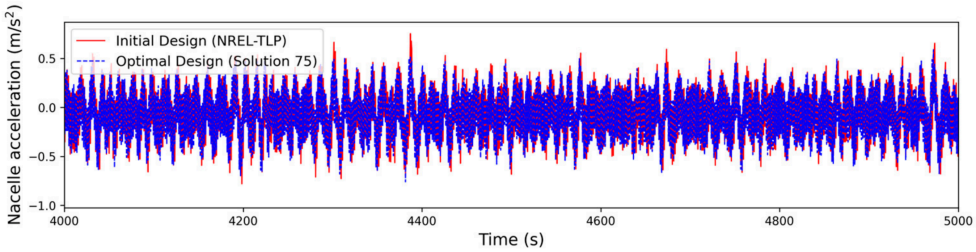

Figure 20. Comparison of time history between optimal solution and initial design (Solution 75).

It is worth noting that the possible tendon slack was also checked for all the sample designs (1215 cases) as well as the Pareto-optimal designs (75 cases) using the instantaneous tendon tensions obtained from FEAMooring in OpenFAST. The post-processing results confirmed that no zero or negative tendon tension occurred in any of the present computed cases. Overall, based on the above three optimization scenarios, the obtained Pareto-optimal designs provide practical guidance for selecting TLP-type FOWT configurations according to different design priorities. For the simultaneous improvement of surge motion and tendon tension, the platform draft and tendon pre-tension should be carefully adjusted, since they directly influence both the hydrodynamic restoring characteristics and the mean tendon load level. For a reduction in tendon tension while maintaining budget, increasing the pontoon length and slightly decreasing the tendon axial stiffness are particularly effective, as they reduce pitch-induced tendon loads and soften the tendon response. For the mitigation of nacelle acceleration, a longer pontoon length, larger platform draft, and relatively high tendon axial stiffness are beneficial, since they help suppress pitch motion and thereby reduce motion-induced acceleration at the nacelle.

4. Conclusions

This study proposed a systematic approach to optimize the design of a TLP-type FOWT with the consideration of both the hydrodynamic performance and the cost-effectiveness. Several parameters related to the hull-form as well as the tendon system were selected as design variables, including the pontoon length (PL), pontoon width (PW), platform draft (PD), diameter of the main column (CD), pre-tension force (Pre) for each tendon, and axial stiffness (EA) per tendon. Nacelle acceleration, surge motion, tension force, and total cost estimation were chosen as the objective functions. To establish the relationship between the design variables and objective functions, a surrogate model based on the response surface method (RSM) was developed. Finally, several sets of Pareto-optimal designs were obtained with the application of the multi-objective evolutionary optimization NSGA-II. The optimization results suggested that:

1. The optimization of tension force and cost index produced a set of optimal designs that achieved substantial improvements in both dynamic tension and cost compared to the baseline design. Among the design variables, pontoon length and axial stiffness were identified as dominant factors. Longer pontoons effectively reduced pitch-induced tension, while slightly decreasing the axial stiffness of tendons helped lower peak tension by softening the tendon response.
2. In the tension–surge motion optimization, the Pareto front exhibited a well-balanced trade-off region, providing a broad range of optimal designs. While surge motion increased slightly, tendon tension showed a clear reduction. Reducing the platform draft and tendon pre-tension extended the effective tendon length and lowered the baseline tension levels, resulting in decreased peak dynamic loads. Pontoon width and main column diameter remained at their lower bounds, indicating limited influence, while pontoon length exhibited a non-monotonic trend.
3. The cost–nacelle acceleration optimization exhibited a two-region Pareto front. In Region I, the cost index reached its minimum with only a modest reduction in nacelle acceleration, primarily driven by increased pontoon length. In Region II, nacelle acceleration decreased more noticeably, supported by an increased draft and continued pontoon extension, accompanied by a slight rise in cost. Throughout both regions, axial stiffness remained at its upper bound, while pontoon width, column diameter, and tendon pre-tension were fixed at their lower bounds to maintain cost efficiency.

The present proposed framework provides a practical design procedure for evaluating the trade-off relationships among the hydrodynamic response, tendon load, and cost-related performance of TLP-type FOWTs. In particular, the obtained Pareto-optimal solutions provide useful preliminary design guidance for selecting appropriate combinations of hull-form parameters and tendon properties while considering the cost contributions of the platform hull, ballast, and tendon system. Therefore, the proposed surrogate model-based optimization framework can support the early-stage design of TLP-type FOWTs by reducing the computational cost and identifying physically meaningful design trends under the considered environmental conditions.

In future work, present proposed optimal designs will be further validated through model test and CFD simulations to capture nonlinear hydrodynamic effects. Additionally, the elasticity of the wind tower will be incorporated as an additional design variable to account for its interaction effect on the entire dynamic response of the FOWT under extreme environmental conditions.

Author Contributions: Conceptualization, Z.S. and B.W.N.; methodology, Z.S.; formal analysis, Z.S.; investigation, Z.S. and B.W.N.; writing—original draft preparation, Z.S.; writing—review and editing, B.W.N.; supervision, B.W.N. All authors have read and agreed to the published version of the manuscript.

Funding: This research was funded by the Korea Agency for Infrastructure Technology Advancement (KAIA), grant funded by the Ministry of Land, Infrastructure, and Transport (Grant RS-2023-00250727) through the Korea Floating Infrastructure Research Center at Seoul National University. This research was also supported by the Korea Institute of Marine Science and Technology Promotion (KIMST), funded by the Ministry of Oceans and Fisheries, Korea (RS-2024-00420405).

Data Availability Statement: The original data presented in the study are openly available in National Renewable Energy Laboratory at https://docs.nrel.gov/docs/fy10osti/46725.pdf (accessed on 1 April 2026).

Conflicts of Interest: The authors declare no conflicts of interest.

References

1. Musial, W.; Spitsen, P.; Duffy, P.; Beiter, P.; Shields, M.; Mulas Hernando, D.; Hammond, R.; Marquis, M.; King, J.; Sathish, S.; et al. *Offshore Wind Market Report: 2023 Edition*; No. NREL/TP-5000-87232; National Renewable Energy Laboratory (NREL): Golden, CO, USA, 2023.
2. Sclavounos, P.; Tracy, C.; Lee, S. Floating offshore wind turbines: Responses in a seastate pareto optimal designs and economic assessment. In *Proceedings of the ASME 2008 27th International Conference on Offshore Mechanics and Arctic Engineering*; ASME: New York, NY, USA, 2008; Volume 48234.
3. Jagdale, S.; Ma, Q.W. Practical simulation on motions of a TLP-type support structure for offshore wind turbines. In *Proceedings of the Twentieth (2010) International Offshore and Polar Engineering Conference*; ISOPE: Mountain View, CA, USA, 2010.
4. Bachynski, E.E.; Moan, T. Design considerations for tension leg platform wind turbines. *Mar. Struct.* **2012**, *29*, 89–114. [CrossRef]
5. Wang, H.F.; Fan, Y.H. Spoke Dimension on the Motion Performance of a Floating Wind Turbine with Tension-Leg Platform. *Shock Vib.* **2016**, *2016*, 8913873. [CrossRef]
6. Sugita, T.; Suzuki, H. A study on TLP hull sizing by utilizing optimization algorithm. *J. Mar. Sci. Technol.* **2016**, *21*, 611–623. [CrossRef]
7. Du Kim, J.; Jang, B.-S. Application of multi-objective optimization for TLP considering hull-form and tendon system. *Ocean Eng.* **2016**, *116*, 142–156. [CrossRef]
8. Karimi, M.; Hall, M.; Buckham, B.; Crawford, C. A multi-objective design optimization approach for floating offshore wind turbine support structures. *J. Ocean Eng. Mar. Energy* **2017**, *3*, 69–87. [CrossRef]
9. Zhang, X.; Song, X.; Qiu, W.; Yuan, Z.; You, Y.; Deng, N. Multi-objective optimization of Tension Leg Platform using evolutionary algorithm based on surrogate model. *Ocean Eng.* **2018**, *148*, 612–631. [CrossRef]
10. Park, H.J.; Song, Z.; Nam, B.W.; Ha, Y.J.; Kim, K.H. Design Optimization of a Tension Leg Platform for Floating Offshore Wind Turbine Based on NSGA-II Algorithm With Surrogate Models. *J. Offshore Mech. Arct. Eng.* **2026**, *148*, 012005. [CrossRef]
11. Matha, D.; Fischer, T.; Kuhn, M.; Jonkman, J. *Model Development and Loads Analysis of a Wind Turbine on a Floating Offshore Tension Leg Platform*; No. NREL/CP-500-46725; National Renewable Energy Lab. (NREL): Golden, CO, USA, 2010.
12. Jonkman, J.M.; Shaler, K. *Fast. Farm User's Guide and Theory Manual*; National Renewable Energy Laboratory: Golden, CO, USA, 2021.
13. Jonkman, J.M.; Matha, D. Dynamics of offshore floating wind turbines—Analysis of three concepts. *Wind Energy* **2011**, *14*, 557–569. [CrossRef]
14. Crozier, A. Design and Dynamic Modeling of the Support Structure for a 10 MW Offshore wind Turbine. Master's Thesis, Institutt for Energi- og Prosessteknikk, Trondheim, Norway, 2011.
15. Carlson, R. Design of Experiments, Principles and Applications, L. Eriksson, E. Johansson, N. Kettaneh- Wold, C. Wikström and S. Wold, Umetrics AB, Umeå Learnways AB, Stockholm, 2000, ISBN 91-973730-0-1, xii + 329 pp. Available online: https://analyticalsciencejournals.onlinelibrary.wiley.com/doi/epdf/10.1002/cem.686 (accessed on 1 April 2026).
16. Cummins, W. The impulse response function and ship motions. *Schiffstechnik* **1962**, *9*, 101–109.
17. Ogilvie, T.F. Recent progress toward the understanding and prediction of ship motions. In *ONR Symposium on Naval Hydrodynamics*; 1964. Available online: https://scispace.com/pdf/recent-progress-toward-the-understanding-and-prediction-of-e6xvn2hkg5.pdf (accessed on 1 April 2026).
18. Vardaroglu, M.; Gao, Z.; Avossa, A.M.; Ricciardelli, F. Validation of a TLP wind turbine numerical model against model-scale tests under regular and irregular waves. *Ocean Eng.* **2022**, *256*, 111491. [CrossRef]
19. Jonkman, J.M. Dynamics Modeling and Loads Analysis of an Offshore Floating Wind Turbine. Ph.D. Thesis, University of Colorado, Boulder, CO, USA, 2007; 237p.
20. Khuri, A.I.; Mukhopadhyay, S. Response surface methodology. *Wiley Interdiscip. Rev. Comput. Stat.* **2010**, *2*, 128–149. [CrossRef]
21. Bezerra, M.A.; Santelli, R.E.; Oliveira, E.P.; Villar, L.S.; Escaleira, L.A. Response surface methodology (RSM) as a tool for optimization in analytical chemistry. *Talanta* **2008**, *76*, 965–977. [CrossRef] [PubMed]
22. Liu, J.-Z.; Weng, L.-P.; Zhang, Q.-L.; Xu, H.; Ji, L.-N. Optimization of glucose oxidase production by Aspergillus niger in a benchtop bioreactor using response surface methodology. *World J. Microbiol. Biotechnol.* **2003**, *19*, 317–323. [CrossRef]
23. Deb, K.; Pratap, A.; Agarwal, S.; Meyarivan, T. A fast and elitist multiobjective genetic algorithm: NSGA-II. *IEEE Trans. Evol. Comput.* **2002**, *6*, 182–197. [CrossRef]
24. Dueñas-Osorio, L.; Basu, B. Unavailability of wind turbines due to wind-induced accelerations. *Eng. Struct.* **2008**, *30*, 885–893. [CrossRef]